Energy Storage Materials 29 (2020) 172–181

Contents lists available at ScienceDirect

Energy Storage Materials

journal homepage: www.elsevier.com/locate/ensm

Polyoxovanadate-polymer hybrid electrolyte in solid state batteries

Mi Zhang [a,1], A-Man Zhang [a,1], Yifa Chen [a,1], Jin Xie [b], Zhi-Feng Xin [a,c], Yong-Jun Chen [a], Yu-He Kan [d], Shun-Li Li [a,**], Ya-Qian Lan [a,***], Qiang Zhang [b,*]

[a] Jiangsu Collaborative Innovation Centre of Biomedical Functional Materials, Jiangsu Key Laboratory of New Power Batteries, School of Chemistry and Materials Science, Nanjing Normal University, Nanjing, 210023, China
[b] Beijing Key Laboratory of Green Chemical Reaction Engineering and Technology, Department of Chemical Engineering, Tsinghua University Beijing, 100084, China
[c] Institute of Molecular Engineering and Applied Chemistry, Anhui University of Technology, Ma'anshan, Anhui, 243002, China
[d] Jiangsu Province Key Laboratory for Chemistry of Low-Dimensional Materials, School of Chemistry and Chemical Engineering, Huaiyin Normal University, Huai'an, 223300, China

ARTICLE INFO

Keywords:
Polyoxometalate
Polymer composite
Nanowire
Ion conductivity
Solid-state battery

ABSTRACT

All-solid-state batteries are emerging as the new generation devices for safe and stable energy storage. However, insufficient ion conductivity of solid electrolyte impairs their practical applications. Herein, a series of fast alkali-ion conductor, polymer/polyoxovanadate hybrid nanowires were fabricated as solid electrolyte by a facile and scalable polyoxovanadate-induced self-assembly method. Combining abundant mobile alkali-ions and terminal oxygen atoms (Lewis base sites) of polyoxovanadates with the ion-migration favoured nanowire assemblage, ultrahigh ion conductivities of universal alkali-ions (25 °C, 3.30×10^{-3}, 2.00×10^{-3}, and 4.55×10^{-3} S cm^{-1} for Li^+, Na^+ and K^+ respectively) with low active energies are achieved. Remarkably, the hybrid solid-state electrolytes were applied in solid-state lithium and potassium batteries, exhibiting remarkable rate capability and comparable cycling stability. The chemical and structural design of polyoxometalate/polymer hybrid solid-state electrolyte shed light on the material design and chemical investigation of next-generation all-solid-state batteries.

1. Introduction

Alkali-ion batteries (AIBs), including Li-ion batteries (LIBs), sodium-ion batteries (SIBs) and potassium-ion batteries (KIBs), have been widely applied in energy storage systems [1,2]. Varies advantages such as the high energy density of LIBs, low cost, and high earth abundance of sodium and potassium in SIBs and KIBs, endowed alkali-ion battery with priority for portable and scaled using [3–5]. However, conventional AIBs generally use liquid organic electrolytes, which leads to some drawbacks such as uncontrollable safety issues and high cost [6]. Concerning these problems, solid-state electrolytes have emerged as a kind of powerful solution for next-generation AIBs [7,8]. In general, typical materials applied in solid-state electrolytes could be categorized into two types: inorganic electrolyte and polymer electrolyte. Inorganic solid-state electrolytes, such as the garnet oxides $Li_xLa_3M_2O_{12}$ [9], NASICON (sodium super ionic conductor)-type phosphates [10] and perovskite-type $Li_{3x}La_{2/3-x1/3-2x}TiO_3$ [11], display high ion conductivity. However, they are many bottlenecks like the poor interfacial contacts in working electrodes [12]. In contrast, solid polymer electrolytes (SPEs), a kind of electrolyte composed of metal salts associated with soft polar polymer matrix, are intended to solve most of the concerning issues encountered with liquid electrolytes [13]. Specially, SPEs with high stability, wide working temperature range and ease of processing show superior performances than inorganic solid-state electrolytes and are regard as one of the most promising materials in next generation solid-state electrolytes [14].

To date, the exploration of SPEs with polymers functionalized with sulfonate (SO_3^-) anions (e.g., polystyrene sulfonate (PSS)) have been intensively investigated [15]. However, PSS possessing similar type of anion moiety in each repeating unit is not easy to reach high ion conductivity, due to the lack of functional groups specified for facilitating the hopping of working ions and sufficient concentration of working ions with high mobility [16]. Therefore, PSS generally presents low ion conductivity (about 10^{-6}-10^{-8} S cm^{-1}) at room temperature and is

* Corresponding author.
** Corresponding author.
*** Corresponding author.
E-mail addresses: slli@njnu.edu.cn (S.-L. Li), yqlan@njnu.edu.cn (Y.-Q. Lan), zhang-qiang@mails.tsinghua.edu.cn (Q. Zhang).
[1] These authors contributed equally

https://doi.org/10.1016/j.ensm.2020.04.017
Received 6 February 2020; Received in revised form 4 April 2020; Accepted 13 April 2020
Available online 19 April 2020

largely lower than the minimum targeted value (10^{-4} S cm^{-1}) required for applicable all-solid-state batteries like LIBs or KIBs [16]. Diverse strategies like mixing PSS with polymer matrices containing soft segments with Lewis base groups [17,18] or to substitute sulfonate anion with other anions (e.g., sulfonylimide) [19] have been explored, yet the performances are still hard to meet the demand of practical applications. This is in part attributed to the lack of morphology-controlled methods that most of previously reported materials based on PSS are sphere nanoparticles or short random nanorods. The ions like alkali-ions step over enormous interface barriers, which eventually results in poor ion conductivity [20]. Besides, in conventional SPEs, most of Li or K salts (e.g., $LiClO_4$, LiTFSI, $KClO_4$ or KPF_6, etc.) dissolving in polymers are mono-ionic lithium salts and are insufficient to provide abundant working ions [21]. Therefore, how to design and construct anionic polymer based materials with well-tuned morphology (e.g., 1D nanowire) and seek new multi-ionic salts possessing sufficient Lewis base sites and working ions is highly demanded to achieve high ion conductivity.

In this contribution, a series of fast alkali-ion conductor, polymer/polyoxovanadate (POVs) hybrid nanowires were fabricated as solid electrolyte by facile and scalable polyoxovanadate-induced self-assembly method (PISA) to solve the problems of conventional polymer electrolyte mentioned above. POVs, as one kind of Polyoxometalates (POMs), possess discrete ionic structure with heteropolyanions and countercations (Li^+, Na^+ and K^+), which manifests themselves to be potential candidates with fast ion conductivity [22–24]. In addition, the large number of terminal oxygen atoms on the external surface of POMs (Lewis base sites) whcih provide abundant sites for alkali-ion transport can address the above concerns of PSS. PISA method utilizing POVs as both co-initiators and construction units to fabricate 1D polyoxovanadates/polystyrene sulfonate (POVs/PSS) hybrid nanowires. POVs play important roles in the preparation of hybrid nanowires and might act as anionic template or structure-directing agents through host-guest supermolecular interactions [25]. The well-controlled 1D nanowires can avoid ion aggregation and can construct well-tuned pathways. This method is applicable in diverse countercations (i.e., Li^+, Na^+, and K^+) and various heteropolyanions (i.e., $[V_{10}O_{28}]^{5-}$, $[V_{15}O_{36}(CO_3)]^{7-}$, and $[V_{34}O_{82}]^{10-}$) with well-tuned POVs loadings and nanowire morphology. Obtained through the PISA method, POVs/PSS hybrid nanowires with aligned 1D morphology can create efficient and continuous ion conductivity pathways to impart these materials with remarkable ion conductivity. Noteworthy, POVs/PSS hybrid nanowires exhibit ultrahigh Li^+, Na^+ and K^+ conductivity and low active energy. The POVs/PSS (e.g., V_{15}/PSS-Li-1 and V_{34}/PSS-K-1) hybrid nanowires with high compatibility with lithium and potassium can be applied as electrolytes in solid-state alkali batteries with remarkable capacities and high cycling stability ($LiFePO_4$|Li batteries, 148 mA h g^{-1} (100 mA g^{-1}), 102.2% retention after 100 cycles; $K_{1.69}Fe[Fe(CN)_6]_{0.90}{\cdot}0.4H_2O$|K batteries, 104.8 mA h g^{-1} (20 mA g^{-1}), 95.6% retention after 20 cycles).

2. Material and methods

2.1. Materials

Sodium-4-vinylbenzenesulfonate ($C_8H_7NaO_3S$) and sodium allysulfonate ($C_3H_5SO_3Na$) were purchased from Shanghai Macklin Biochemical Co., Ltd. Sodium persulfate ($Na_2S_2O_8$), 2-acrylamido-2-methylpropane sulfonic acid ($C_7H_{13}NO_4S$), potassium metavanadate (KVO_3) and lithium chloride (LiCl) were obtained from Aladdin Co., Ltd. Potassium persulfate ($K_2S_2O_8$), sodium carbonate anhydrous (Na_2CO_3), potassium carbonate anhydrous (K_2CO_3) were purchased from Shanghai LingFeng Chemical Reagent Co., Ltd. 2-propanol, hydrazine sulfate ($N_2H_4{\cdot}H_2SO_4$), hydrazine hydrate (HCl, 36%) and ammonium persulfate ($(NH_4)_2S_2O_8$) were acquired from Sinopharm Chemical Reagent Co., Ltd. Vanadium oxide (V_2O_5) was purchased from Alfa Aesar (China) Chemicals Co., Ltd. Lithium carbonate (Li_2CO_3) was bought from XiLong Chemical Co., Ltd. Lithium bis(trifluoromethanesulphonyl) imide (LiTFSI) was obtained from Adamas Reagent Co., Ltd.

2.2. Syntheses of Li_7V_{15}, HNa_6V_{15}, HK_5V_{10}, K_7V_{15} and $K_{10}V_{34}$

Li_7V_{15} (the formula is $Li_7[V_{15}O_{36}(CO_3)]{\cdot}39H_2O$) was prepared following the reported method in reference [26]. 5.88 g Li_2CO_3 (79.60 mmol) was dissolved in 150 mL H_2O under stirring to achieve homogeneous solution. 12 g of V_2O_5 (65.90 mmol) was added portion wise in the solution under stirring and further continue stirring for 5 min. After filtration off the residues, the solution in a 300 mL Erlenmeyer flask was heated after the temperature reach at 90 °C. After 1.5 g hydrazine sulfate (11.5 mmol) as added portionwise in the solution under stirring and the flask was kept heating at 90 °C for 1 h. After filtration, the obtained greenish-black solution was shaking with 50 mL of 2-propanol after cooling to 20 °C. After placing the solution at 5–7 °C for 2-3d, black crystals were collected after washing with 2-propanol and drying under vacuum. The syntheses of HNa_6V_{15} (the formula is $HNa_6[V_{15}O_{36}(CO_3)]{\cdot}nH_2O$) and K_7V_{15} (the formula is $K_7[V_{15}O_{36}(CO_3)]{\cdot}nH_2O$) were similar to that of Li_7V_{15} except that Na_2CO_3 or K_2CO_3 was used to replace Li_2CO_3.

HK_5V_{10} (the formula is $HK_5[V_{10}O_{28}]{\cdot}10H_2O$): KVO_3 (3.39 g) is dissolved in de-ionized water (100 mL); then, 4 M HCl is added to acidify the solution until a pH of 4.8 is reached. The solution is filtered and additional HCl is added to maintain a pH of around 4.5. Subsequently, ethanol (95%, 200 mL) was added to precipitate bulk product, which is then filtrated and air-dried.

$K_{10}V_{34}$ (the formula is $K_{10}[V_{34}O_{82}]{\cdot}20H_2O$) was prepared following the reported method in reference [27]. KVO_3, (3.45 g, 25.0 mmol) was dissolved in H_2O (50 mL) at 90 °C in a 100 mL Erlenmeyer flask. The clear solution was then treated with 182 μL of hydrazinium hydroxide (100%, 3.75 mmol) and kept at 90 °C. After 1 h, the pH of the above solution was adjusted to 3.8 by addition of glacial acetic acid. After a further 2 h the solution was filtered hot, the filtrate kept at 90 °C for 3 h and finally cooled to room temperature. After standing for 1 d, needle-shaped crystals were filtered off, washed with a little 50% aqueous 2-propanol, and dried in air.

2.3. Syntheses of V_{15}/PSS-Li-n ($n = 1$–4)

Taking the synthesis of V_{15}/PSS-Li-1 for example, $C_8H_7NaO_3S$ (2.06 g, 10.00 mmol), $(NH_4)_2S_2O_8$ (0.40 g), Li_7V_{15} (1.08 g, 0.50 mmol) were mixed and dissolved in 60 mL distilled water under stirring. Subsequently, the solution was transferred into a 100 mL three neck flask and heated with an oil bath at 80 °C for 20 h. After cooling to room temperature, the as-synthesized sample was collected by filtration. The as-synthesized sample was re-dispersed in LiCl aqueous solution (50 mg mL^{-1}) at 50 °C for ion exchange. The solution was changed with the fresh LiCl solution every 48 h and the procedure was repeated for three times. After washing with water for several times and drying under vacuum at 100 °C overnight, V_{15}/PSS-Li-1 sample was successfully obtained. To adjust the loadings of the Li_7V_{15} in V_{15}/PSS-Li, the moral ratio of POV/SS is tuned from 1 : 20 to 1 : 200 and resulted in 84.1, 80.5, 77.2, and 74.9 wt% of Li_7V_{15} loadings in the final V_{15}/PSS-Li-n (n = 1–4) (calculated based on V and C elements amount determined by EDS tests). In this research, we also tried to synthesize samples with higher Li_7V_{15} content, however the obtained samples were in liquid-phase. Therefore, V_{15}/PSS-Li with 84.1 wt% Li_7V_{15} loading was the highest POV content sample reported in this study. For the synthesis of PSS-Li, commercial PSS-Na powder was dispersed in a 15 wt% LiTFSI contented N,N-Dimethylformamide (DMF) solution (100 mL, 10 mg mL^{-1}) at 50 °C for ion exchange. The solution was changed with the fresh LiTFSI solution every 48 h and the procedure was repeated for three times. The sample was collected after washing with DMF for several times and drying under vacuum at 100 °C overnight. For the gram-level production, the precursor amounts of V_{15}/PSS-Li-1 were expanded to tenfold of the original ones. Appling similar conditions except that the reaction time adjusted to 40 h, about 8.7 g of V_{15}/PSS-Li-1 (87% yield) was produced.

2.4. Synthesis of V_{15}/PSS-Na-n, V_{10}/PSS-K-1, V_{15}/PSS-K-1 and V_{34}/PSS-K-n (n = 1–4)

The syntheses of V_{15}/PSS-Na-n, V_{10}/PSS-K-1, V_{15}/PSS-K-1 and V_{34}/PSS-K-n (n = 1–4) were similar to that of V_{15}/PSS-Li-n (n = 1–4) except that HNa_6V_{15}, $Na_2S_2O_8$ and HK_5V_{10}, K_7V_{15}, $K_{10}V_{34}$, $K_2S_2O_8$ were used to replace Li_7V_{15} and $(NH_4)_2S_2O_8$, respectively.

2.5. Material characterization

Power X-Ray diffraction (PXRD) patterns were recorded on a D/max 2500 VL/PC diffractometer (Rigaku SmartLab, Japan) equipped with graphite mono-chromatized Cu Kα radiation (λ = 1.54060 Å). The FTIR was collected on a Nexus 670 spectrometer. The TGA was carried out by using a DSC 800 from PerkinElmer under N_2 flowing with a heating rate of 10 °C min^{-1} from room temperature to 450 °C. The Raman measurement was performed on Lab-RAM HR800. The morphology analyses of the samples were conducted on a scanning electron microscope (SEM, JSM-7600F) at an acceleration voltage of 10 kV and transmission electron microscopy (TEM) on JEOL-2100F apparatus at an accelerating voltage of 200 kV. The Elemental mapping and energy dispersive X-ray spectroscopy (EDX) were examined with JSM-5160LV-Vantage typed energy spectrometer. X-ray photoelectron spectroscopy (XPS) was measured on scanning X-ray microprobe (PHI 5000 Verasa, ULAC-PHI, Inc.) using Al kα radiation and the C1s peak at 284.8 eV as internal standard. The mass spectroscopy (MS) was carried out on Bruker UltrafleXtreme MALDI-TOF/TOF instrument. The cycling and rate performances tests were carried out on a LAND CT2001A (China) battery measurement system with a cutoff voltage window of 4.5–2 V vs Li^+/Li. Cyclic voltammetry (CV, 1 mV s^{-1}) and linear sweep voltammetry (LSV, 1 mV s^{-1})) were collected on a electrochemical workstation CHI 660D (Shanghai, China). The electrochemical impedance spectroscopy (EIS) curves studies were measured at an impedance/gain-phase analyzer (Solartron S1 1260) over a frequency range from 10^7 to 0.1 Hz with an input voltage of 100 mV.

Single-Crystal X-ray Crystallography: The diffraction data of HNa_6V_{15} and K_7V_{15} were collected on Bruker AXS Apex Duo diffractometer with graphite monochromatized (Mo Kα, λ = 0.71069 Å) X-radiation and a CCD area detector at 293 K. Raw frame data were integrated with the SAINT program. A multi-scan absorption correction was applied with the program SADABS. All structures were solved by the intrinsic Phasing method with SHELXT [28] and refined with the full-matrix least-squares technique with SHELXL [29] under $Olex^2$ software [30]. All non-hydrogen atoms were refined with anisotropic displacement parameters. The detailed structure parameters and crystallographic data are shown in Table S1. CCDC numbers of HNa_6V_{15} and K_7V_{15} are 1866480 and 1866479, respectively. These data can be obtained free of charge from The Cambridge Crystallographic Data Centre.

2.6. Electrochemical measurements

Ion conductivity was measured using EIS tests (Solartron S1 1260). The samples were pressed into round pellets (diameter, 4 mm and thickness, 2.5 mm). During the test, the pellet was placed between two gold sticks under Ar atmosphere to eliminate the effect of water and oxygen. The frequency range applied was from 10^7 to 0.1 Hz and the AC amplitude was 100 mV. Ion conductivity was calculated based on the formula of $L/(R \times A)$, R (Ohm) stands for the ionic resistivity measured through the end point of the semicircle of EIS spectra, L (cm) is the thickness of pellet and A (cm^2) is the area of the pellet. To measure the activation energies, EIS tests of the sample at different temperatures were conducted and the values of activation energies were calculated based on the Arrhenius formula.

For electrochemical compatibility test, V_{15}/PSS-Li-1 or V_{34}/PSS-K-1 was fabricated into membrane. V_{15}/PSS-Li-1 or V_{34}/PSS-K-1 powder was dispersed in the DMF solution of polyvinylidene fluoride (PVDF) (0.2 g mL^{-1}) under ultrasonic for 30 min and further stirring for 12 h (weight ratio, V_{15}/PSS-Li-1 or V_{34}/PSS-K-1: PVDF = 1 : 3). The obtained solution was casted onto a glass pellet (10 cm × 10 cm) with defined thickness (400 μm) and then dried under vacuum at 80 °C for 12 h. After peeling from the glass pellet, V_{15}/PSS-Li-1 or V_{34}/PSS-K-1 based PVDF membrane (7.5 cm × 8.0 cm × 50 μm) was obtained. For the CV and LSV tests, lithium foils were used as reference/counter electrodes, stainless-steel plates were applied as the working electrodes and V_{15}/PSS-Li-1 or V_{34}/PSS-K-1 based PVDF membrane (crushed into round pellet with a diameter of 18 mm) were utilized as electrolyte membrane. The CV tests were performed in the potential range of −0.2–3 V (vs Li^+/Li) and −0.5–3 V (vs K^+/K) and the LSV tests were carried out in the potential range of 2–5 V (vs Li^+/Li) and 2.5–4.5 V (vs K^+/K) at a scan rate of 1 mV s^{-1} on electrochemical workstation CHI 660D (Shanghai, China).

For the electrochemical tests of solid-state batteries, the cathode was prepared by mixing $LiFePO_4$ or $K_{1.69}Fe[Fe(CN)_6]_{0.90}{\cdot}0.4H_2O$, acetylene black (Super-P), PVDF (70 : 20: 10 by weight) in N-methyl-2-pyrrolidinone solvent and ground in a mortar for minutes. $K_{1.69}Fe[Fe(CN)_6]_{0.90}{\cdot}0.4H_2O$ was prepared following the reported method in reference [31]. After coating the obtained slurries on aluminum foils collector, the electrodes were dried at 90 °C in vacuum for 24 h to remove the solvent. The active material loading of the cathode was about 2 mg cm^{-2}. A lithium foil and V_{15}/PSS-Li-1 or V_{34}/PSS-K-1 based PVDF membrane were used as the counter electrode and electrolyte, respectively. One drop (about 8 μL) of electrolyte was added to ensure permeation into the electrode matrix. The solid-state battery (Li/(V_{15}/PSS-Li-1)/$LiFePO_4$) or (K/(V_{34}/PSS-K-1)/$K_{1.69}Fe[Fe(CN)_6]_{0.90}{\cdot}0.4H_2O$) was assembled in an argon-filled glove box and the cycling and rate performance tests were evaluated on a Land CT2001A measurement system.

3. Results and discussion

3.1. Structure and characterization of POVs and POVs/PSS hybrid nanowires

The syntheses of POVs/PSS hybrid nanowires are schematically described in Fig. 1 (detailed synthesis procedures are illustrated in the methods section). Five kinds of POVs (i.e., Li_7V_{15}, HNa_6V_{15}, HK_5V_{10}, K_7V_{15}, and $K_{10}V_{34}$) that possess abundant countercations and terminal oxygen atoms (Lewis base sites) are specially proposed (Fig. 2A–B and Figs. S1–S6). Except for Li_7V_{15}, HK_5V_{10}, and $K_{10}V_{34}$, two new POVs (i.e., HNa_6V_{15} and K_7V_{15}) crystals are synthesized through hydrothermal methods. Proved by powder X-ray diffraction (PXRD) tests, the obtained Li_7V_{15}, HNa_6V_{15}, HK_5V_{10}, K_7V_{15}, and $K_{10}V_{34}$ match well with the simulated ones (Fig. 2A–B and Fig. S6). The well-defined structures are further characterized by Fourier-transform infrared (FT-IR) (Fig. S7A) and Raman characterizations (Fig. S7B). Detailed crystal information is illustrated in Table S1. Li_7V_{15}, HNa_6V_{15}, and K_7V_{15} exhibit identical spherical heteropolyanion $[V_{15}O_{36}(CO_3)]^{7-}$ while different countercations. On the contrary, HK_5V_{10}, K_7V_{15}, and $K_{10}V_{34}$ possess various heteropolyanion ($[V_{10}O_{28}]^{5-}$, $[V_{15}O_{36}(CO_3)]^{7-}$, and $[V_{34}O_{82}]^{10-}$) and same countercations. There are a large number of oxygen atoms (Lewis base sites) on the surface of $[V_{10}O_{28}]^{5-}$, $[V_{15}O_{36}(CO_3)]^{7-}$, and $[V_{34}O_{82}]^{10-}$ which render strong interactions with polymers thus generating enormous mobile ions and creating continuous ion conducting pathways in the hybrid materials [32].

The pattern of V_{15}/PSS-Li displays remained peaks (e.g., 8.14°, 24.9°, 25.7° and 34.6°) of Li_7V_{15} (Fig. 2A). As for commercial PSS-Li, there is no diffraction peak observed in the PXRD test, indicating a mainly amorphous phase (Fig. S9). The FT-IR and Raman spectra further confirm the presence of PSS-Li and Li_7V_{15} components in V_{15}/PSS-Li (Fig. S10). Similar results are also detected in V_{15}/PSS-Na, V_{10}/PSS-K, V_{15}/PSS-K and V_{34}/PSS-K verified by PXRD, FT-IR and Raman tests (Fig. 2B and Figs. S6 and S11). Further proven by X-ray photoelectron spectroscopy (XPS) tests, the valence of POVs in POVs/PSS can all be remained after

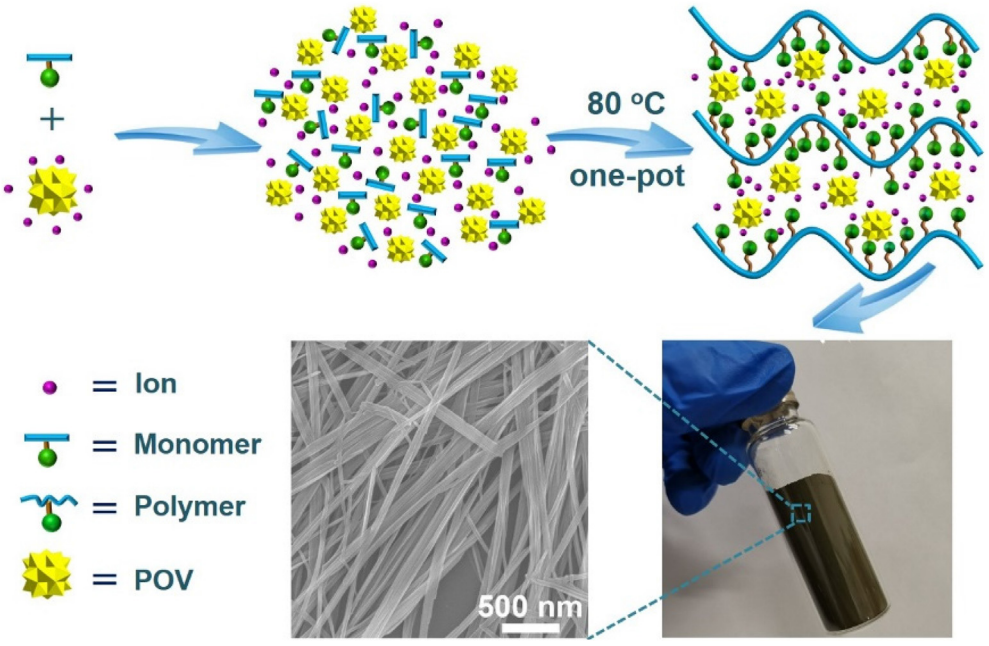

Fig. 1. The schematic illustration of the formation of POVs/PSS.

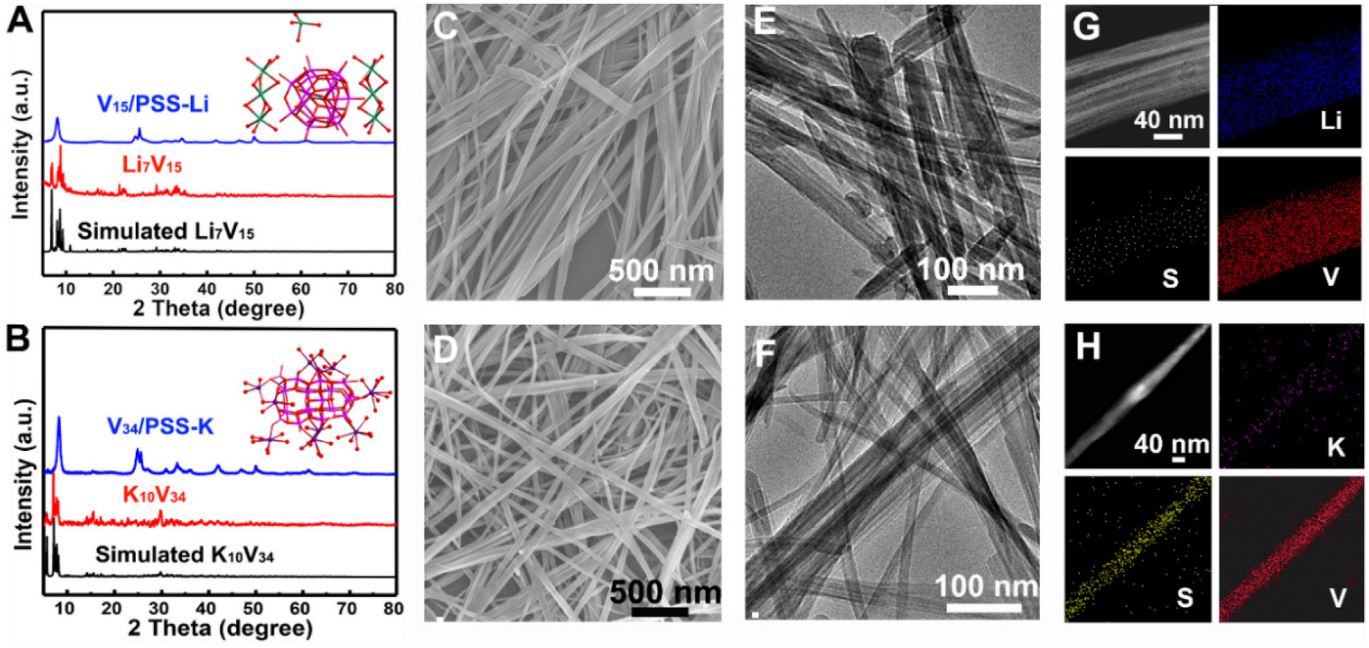

Fig. 2. The crystal structures, PXRD patterns, SEM and TEM images of POVs/PSS. (A) PXRD patterns of simulated Li_7V_{15}, Li_7V_{15} and V_{15}/PSS-Li-1 and crystal structure of Li_7V_{15} (inset). (B) PXRD patterns of simulated $K_{10}V_{34}$, $K_{10}V_{34}$ and V_{34}/PSS-K-1 and crystal structure of $K_{10}V_{34}$ (inset). (C), (D) SEM images of V_{15}/PSS-Li-1 and V_{34}/PSS-K-1. (E), (F) TEM images of V_{15}/PSS-Li-1 and V_{34}/PSS-K-1. (G), (H) EDX elemental mapping of V_{15}/PSS-Li-1 and V_{34}/PSS-K-1.

polymerization (Figs. S12–S14). The mass spectroscopy, PXRD and FT-IR of POVs/PSS and POVs are performed to verify the existence of POVs in POVs/PSS (Figs. S15–S18). In addition, energy dispersive X-ray spectroscopy (EDX) elemental mapping tests are conducted to further confirm the incorporation of POVs into POVs/PSS hybrid materials. Taking V_{15}/PSS-Li for instance, Li, S, and V elements are uniformly distributed in V_{15}/PSS-Li nanowires (Fig. 2G). Similar results are also detected for V_{15}/PSS-Na, V_{10}/PSS-K, and V_{15}/PSS-K (Fig. 2H and Figs. S19C, S20C,F).

To investigate the impact of POVs contents on the resulting hybrid nanowires, POVs/PSS with different contents of Li_7V_{15}, HNa_6V_{15}, and K_7V_{34} (denoted as V_{15}/PSS-Li-n, V_{15}/PSS-Na-n and V_{34}/PSS-K-n, n = 1–4) are prepared and verified by PXRD tests (Figs. S22–S24). Detailed synthesis procedures and relative loadings of POVs in POVs/PSS hybrid materials are illustrated in the methods section. To find out the self-assemblage 1D nanowires structure of POVs/PSS, a series of morphological study of V_{15}/PSS-Li-n (n = 1–4), V_{15}/PSS-Na-n (n = 1–4) and V_{34}/PSS-K-n (n = 1–4) are detected by SEM and TEM tests (Figs. S25–S27). Taking V_{15}/PSS-Li-n for example, V_{15}/PSS-Li-n show nanowires or nanorods morphology. The lengths of the nanowires can be tuned from about 4.2 μm to 200 nm and the diameters of slightly decreased from 42 nm to 31 nm with the decreased loadings from V_{15}/PSS-Li-1 (84.1 wt%) to V_{15}/PSS-Li-4 (74.9 wt%) (Table S2). Interestingly, with the decrease of

Li_7V_{15} loadings, the aligned nanowires of V_{15}/PSS-Li-n become shorter and shorter and finally results in short random nanorods for V_{15}/PSS-Li-4 (Fig. S25). Similar morphology changing from aligned nanowires to short random nanorods can also be detected in V_{15}/PSS-Na-n and V_{34}/PSS-K-n (Fig. 2 and Figs. S26–S27). Cui et al. have demonstrated that polymer electrolytes with aligned Li^+-conductive nanowires exhibit a significant enhancement of ion conductivity compared with random nanowire or nanoparticle-based electrolytes [33]. In contrast with the sizes about 28 and 22 μm of the commercial PSS-Na and PSS-Li or V_{15}/PSS-Li-2, 3, 4, the V_{15}/PSS-Li-1 have the biggest and longest diameter and length, which can create continuous ionic transport pathways to longest distances (Fig. 2C and Figs. S21 and S25). We suppose that the well-tuned morphology from nanowires to nanorods for POVs/PSS might have excellent performances in material durability or ion conductivity.

Thermal stability is a key factor to evaluate the practical applications of SPEs [34]. Thermogravimetric analysis (TGA) and differential scanning calorimetry (DSC) profiles are carried out to study the thermal stability of V_{15}/PSS-Li-n, V_{15}/PSS-Na-n and V_{34}/PSS-K-n (n = 1–4) (Figs. S28–S30). Taking V_{15}/PSS-Li-n for example, the decomposition temperatures of V_{15}/PSS-Li-n (n = 1–4) electrolyte at about 200 °C are observed that can meet the requirements of practical applications in LIBs (The highest temperature limits, about 60–80 °C) [35]. Besides, the decomposition temperatures of V_{15}/PSS-Na-n and V_{34}/PSS-K-n are about 250 and 200 °C, respectively. In DSC profiles (tested from −50 to 200 °C), taking V_{15}/PSS-Li-1 for instance, the glass transition (T_g) and melting temperature (T_m) of V_{15}/PSS-Li-1 are 58.2 and 168.3 °C, respectively. The high thermal stability of these hybrid materials sets fundamental basis for potential SPEs applications.

3.2. The electrocatalytic performance of POVs/PSS

Because of the 1D aligned nanowire morphology, enough counteractions and high thermal stability of these POVs/PSS, they might be excellent Li^+, Na^+, or K^+ conductors. To support the hypothesis, electrochemical impedance spectroscopy (EIS) measurements are performed under Ar atmosphere to evaluate the intrinsic ion conductivity of POVs/PSS electrolyte. Taking V_{15}/PSS-Li for example, V_{15}/PSS-Li hybrid nanowires yield Nyquist plot consisting of single, slightly depressed semicircle (Fig. 3A and Fig. S32). With the increase of Li_7V_{15} loadings (from 74.9 to 84.1 wt%) and the change of relative morphology from short random nanorods (V_{15}/PSS-Li-4, diameter, ~32 nm and length, ~200 nm) to aligned nanowires (V_{15}/PSS-Li-1, diameter, ~42 nm and length, ~4.2 μm), V_{15}/PSS-Li possess higher ion conductivity (from V_{15}/PSS-Li-4, 4.89×10^{-4} to V_{15}/PSS-Li-1, 3.30×10^{-3} S cm^{-1}) (Fig. 3C, Fig. S34 and Table S3). Generally, the morphology of PSS based materials are presented as nanoparticles or short random nanorods. The interface barriers of nanoparticles or short random nanorods will cause inevitable obstacles during ion conductivity and impair the improvement of performances for PSS (Fig. S35). Obtained through the PISA method, POVs/PSS hybrid nanowires with aligned 1D morphology can create efficient and continuous ion conductivity pathways to impart these materials with remarkable ion conductivity (Fig. S35). This all indicates that the morphology-controlled PISA method indeed has impact on the performances of the hybrid materials. Similar results are detected for V_{15}/PSS-Na-n and V_{34}/PSS-K-n with the enhancement of POVs loadings (Fig. 3B and Figs. S36 and S39). After the modification of POVs types and loadings, the best performances of Li^+, Na^+ and K^+ conductivity are 3.30×10^{-3} S cm^{-1} (V_{15}/PSS-Li-1), 2.00×10^{-3} S cm^{-1} (V_{15}/PSS-Na-1) and 4.55×10^{-3} S cm^{-1} (V_{34}/PSS-K-1) at room temperature, respectively. In addition, V_{34}/PSS-K-1 (4.55×10^{-3} S cm^{-1}) exhibits better K^+ conductivity than V_{10}/PSS-K-1 (3.22×10^{-4} S cm^{-1}) and V_{15}/PSS-K-1 (1.23×10^{-3} S cm^{-1}) (Fig. 3B - D and Fig. S37). It might be attributed to the larger amount of terminal oxygen atoms (Lewis base sites) and counteractions of $K_{10}V_{34}$ compared with HK_5V_{10} and K_7V_{15} (Fig. 6A). With more terminal oxygen atoms (Lewis base sites) and countercations in the structure, the samples might provide more sites for ion transport and thus

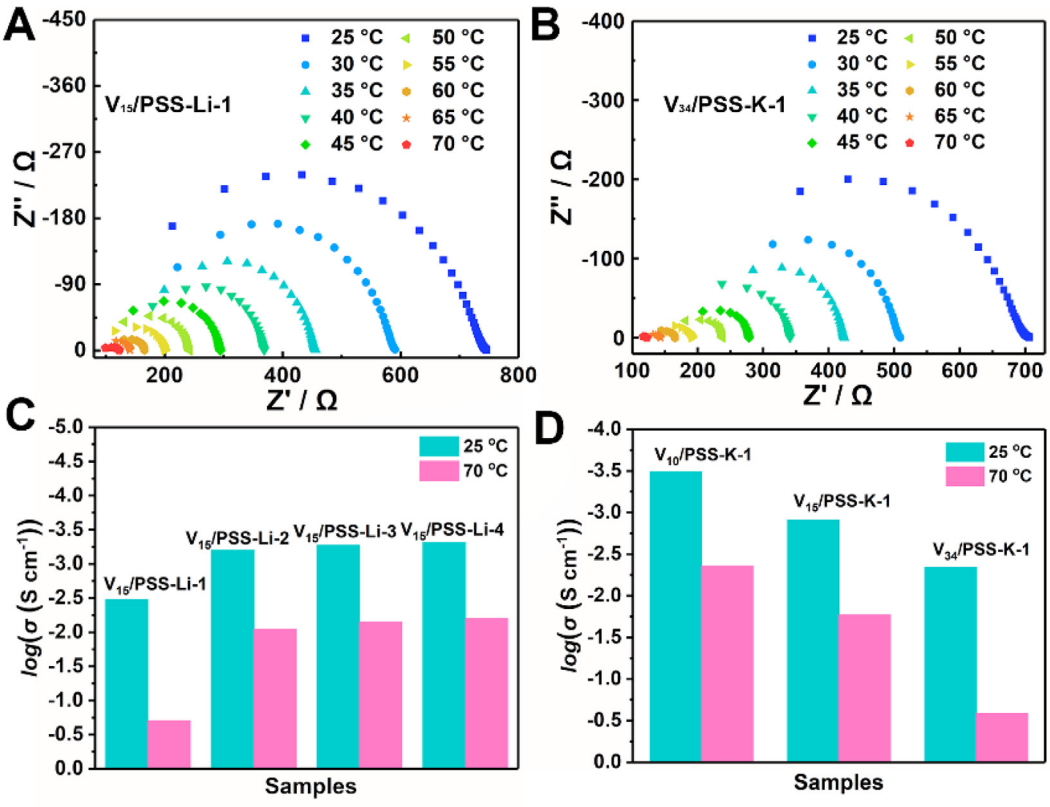

Fig. 3. Impedance spectra of different samples. Impedance spectra of (A) V_{15}/PSS-Li-1, (B) V_{34}/PSS-K-1, (C) Comparison of the ion conductivity among V_{15}/PSS-Li-n (n = 1–4) and (D) Comparison of the ion conductivity among V_{10}/PSS-K-1, V_{15}/PSS-K-1, and V_{34}/PSS-K-1.

further contributing to the enhancement of ion conductivity. It is worthy to note that, these materials show ultrahigh performances in reported polymer based materials for Li^+, Na^+ and K^+ conductivity at room temperature (Fig. 6B and Tables S5–S7) [36–38]. Considering that the 4 and 3 orders of magnitude lower conductivity of pristine PSS-Li and Li_7V_{15} at room temperature (Figs. S40–S41 and Table S3), the assemblage and hybrid strategy are of great significance in creating efficient and continuous ion conductivity pathways to impart these materials with remarkable ion conductivity. In addition, similar results are also detected for V_{15}/PSS-Na-1 and V_{34}/PSS-K-1 in comparison with their relative contrast samples. (Figs. S42–S44 and Table S3). Except for room temperature, the ion conductivity properties at different temperatures are also investigated. The temperature dependence experiments of the ion conductivity for V_{15}/PSS-Li, V_{15}/PSS-Na, V_{10}/PSS-K, V_{15}/PSS-K, and V_{34}/PSS-K are tested over the temperature range of 25–70 °C (Fig. 3A–B and Figs. S32, S36, S39). Notably, these samples mentioned above all follow Arrhenius-like behavior and V_{15}/PSS-Li-1 and V_{34}/PSS-K-1 present activation energy values of 0.50 and 0.59 eV, respectively. (Figs. S31 and S38). The results might be explained that alkali-ions in POVs/PSS are transported by the hopping of working ions between sulfonate groups of PSS and the external oxygen (Lewis base sites) atoms of POVs, similarly to the Grotthuss mechanism in proton conductivity [39]. The PXRD analyses after these measurements display no significant change, which shows that V_{15}/PSS-Li, V_{15}/PSS-Na and V_{34}/PSS-K can maintain the structural integrity during ion transport measurements (Figs. S22–S24).

Not only the conductivity of ions, but the compatibility of interface matters for a stable solid electrolyte is of significant importance with respect to their potential applications. To investigate the compatibility of these materials with lithium, the plating/stripping behavior of lithium across the V_{15}/PSS-Li-1 electrolyte is evaluated by cyclic voltammetry (CV) with stainless steel working electrode and lithium metal reference electrode and V_{15}/PSS-Li-1 based PVDF membrane (25 wt%, 40 μm in thickness) as electrolyte membrane (inset of Fig. 4A). The strong reduction peak at −0.20 V (vs. Li^+/Li) in the negative scan corresponds to the plating of lithium and the oxidation peak at 0.11 V (vs. Li^+/Li) suggests the stripping of lithium from the working electrode in the following positive scan (Fig. 4A) [38]. Moreover, a linear sweep voltammetry (LSV) is tested to evaluate the electrochemical window of V_{15}/PSS-Li-1 in the potential range from 2 to 5 V at the scan rate of 1 mV s^{-1} (Fig. 4B). V_{15}/PSS-Li-1 electrolyte is stable up to 4.50 V (vs. Li^+/Li). Considering the common electrochemical window applicable in lithium ion battery below 4 V, the wide potential range of V_{15}/PSS-Li-1 holds promise in the practical applications of lithium ion batteries [40,41]. Above all, the plating/stripping and LSV tests demonstrate that V_{15}/PSS-Li-1 is a kind of promising alternatives exhibiting high compatibility with lithium for solid polymer electrolytes.

Additionally, ion transference number is measured to find out the ion selectivity of V_{15}/PSS-Li-1 electrolyte, which is relative to the stability of solid electrolyte. The t_{Li+} of V_{15}/PSS-Li-1 is measured using a Li|V_{15}/PSS-Li-1|Li symmetric cell by potentiostatic polarization method [42] with a constant polarization potential of 10 mV at 25 °C [40,43]. The t_{Li+} of V_{15}/PSS-Li-1 is calculated to be 0.7 (Fig. S45). This result is close to 1, indicative of single Li-ion conducting behavior, which is attributed to the huge volume of the polyanions (PSS–Li and POVs) [44,45]. High t_{Li+} (0.7) can prevents anion movement and accumulation which eliminates the polarization effects present in electrolytes. To evaluate the impedance and Li^+ transport capability across V_{15}/PSS-Li-1 and Li metal interface, the direct current (DC) Li plating/stripping experiment is measured referred to the literatures [40,43]. The time-dependent voltage profile of the Li|V_{15}/PSS-Li-1|Li nonblocking cell under current densities of 0.05 and 0.1 mA cm^{-2} is displayed in Fig. S46. The voltage profile in each cycle is quite smooth and remains stable over 200 cycles. Moreover, small polarization voltages of ±103 and ±186 mV are observed for 0.05 and 0.1 mA cm^{-2}, respectively, indicating low interfacial impedance between the V_{15}/PSS-Li-1 and lithium.

Combing high compatibility with lithium and ultrahigh Li^+ conductivity in polymer-based electrolytes together, V_{15}/PSS-Li-1 have potential to be efficiently applied as electrolytes in solid-state lithium batteries. As a proof-of-concept, V_{15}/PSS-Li-1 electrolyte is successfully applied (V_{15}/PSS-Li-1 based PVDF membrane, 25 wt%, 40 μm in thickness) in a solid-state lithium battery (Li/(V_{15}/PSS-Li-1)/$LiFePO_4$) (inset of Fig. 4B) and the battery exhibits excellent rate capability and cycling performances (Figs. S47–S50). As shown in Fig. 4C, the first discharge capacity of the battery (Li/(V_{15}/PSS-Li-1)/$LiFePO_4$) is 145.0 mA h g^{-1} at 100 mA g^{-1}.

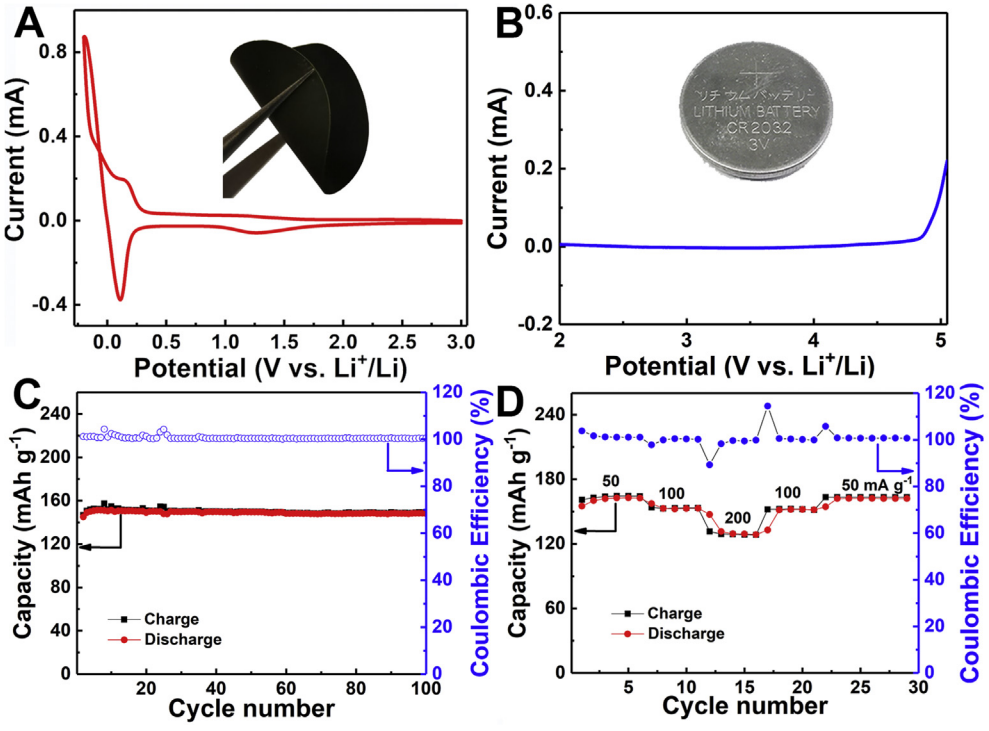

Fig. 4. The CV, LSV plot and solid-state lithium battery tests of V_{15}/PSS-Li-1. (A) The plating/striping behavior at scan rate of 1 mV s^{-1} and photograph of V_{15}/PSS-Li-1 based PVDF membrane (inset). (B) LSV plot at scan rate of 1 mV s^{-1} and photograph of coin cell (inset). (C) Cycling performance of the solid-state lithium battery (Li/(V_{15}/PSS-Li-1)/$LiFePO_4$) at the current density of 100 mA g^{-1}. (D) The rate performances of solid-state lithium battery (Li/(V_{15}/PSS-Li-1)/$LiFePO_4$) at different current densities from 50 to 200 mA g^{-1}.

After 100 cycles, the discharge capacity is 148.2 mA h g^{-1} (102.2% retained). Moreover, high capability (164.5, 153.3, 129.0, 152.5 and 163.4 mA h g^{-1} at current rates of 50, 100, 200, 100 and 50 mA g^{-1}, respectively) are also achieved for the solid-state battery at diverse current rates (Fig. 4D). These results indicate that POVs/PSS hybrid nanowires hold great promise in the applications of electrolytes in solid-state batteries.

Similarly, V_{34}/PSS-K-1 with K^+ also displayed high stability and compatibility with potassium anode and common cathode. In Fig. 5A, the curve shows a pair of strong reduction and oxidation peaks. The sharp reduction peak in the negative scan at −0.5 V (vs. K/K^+) reveals the plating of potassium on working electrode. In the subsequent positive scan, the oxidation peak at 0.37 V (vs. K/K^+) indicates the striping of potassium from stainless steel. No obvious side reaction is shown between 2.5 V and 4.25 V (Fig. 5B), indicating that the potential window of V_{34}/PSS-K-1 is wide enough to meet the demand of the $K_{1.69}Fe[Fe(CN)_6]_{0.90}{\cdot}0.4H_2O$ cathode electrode for potassium battery. The cycling stability of $K_{1.69}Fe[Fe(CN)_6]_{0.90}{\cdot}0.4H_2O$ cathode with V_{34}/PSS-K-1 versus the solid-state electrolyte at 20 mA g^{-1} is shown in Fig. 5C. The discharge capacity of the battery ($K/(V_{34}$/PSS-K-1)/$K_{1.69}Fe[Fe(CN)_6]_{0.90}{\cdot}0.4H_2O$) reaches 104.8 mA h g^{-1} after 20 cycles. The capabilities received at 20, 50, 100 and 200 mA g^{-1} are 110, 90, 70 and 50 mA h g^{-1}, respectively (Fig. 5D).

3.3. The mechanism of ion conductivity for POVs/PSS

In this method, POVs acting as construction unit are uniformly dispersed in the 1D nanowire and might interact with polymers to exhibit positive effect on the enhancement of ion conductivity. To support the hypothesis, ^{7}Li static solid-state nuclear magnetic resonance (NMR) spectra is performed. The resonance peak of V_{15}/PSS-Li-1 (1.90 ppm) is found to shift to positive positions compared with pure Li_7V_{15} by −0.38 ppm, which implies that the incorporation of PSS can lead to different Li^+ chemical environments in V_{15}/PSS-Li-1 (Fig. S53) [46,47]. The local environments of possible ion within POV/PSS are marked in grey in Fig. 6A. In addition, POVs with more contercations and terminal oxygen atoms (Lewis base sites) tend to present higher ion conductivity for POVs/PSS. As proved by the performances of HK_5V_{10}, K_7V_{15} and $K_{10}V_{34}$ based POVs/PSS, POVs with more terminal oxygen atoms (Lewis base sites) can provide more sites for ions transport and thus further contributing to the enhancement of ion conductivity (Fig. 6A).

As mentioned above, the unique PISA method can generate 1D POVs/PSS hybrid nanowires with excellent ion conductivity. This can be contributed to the superiority of this powerful method. Firstly, POVs can act as new multi-ion salts to provide abundant working ions with high mobility to create efficient pathways for ion transport. Secondly, POVs can act as structure-directing agents to control the morphology of POVs/PSS with aligned 1D nanowire morphology, which can create continuous ion transport pathways to reduce the interface barriers. Thirdly, the possible interactions between sulfonate groups of PSS and external oxygen atoms of POVs would provide abundant sites for Li^+, Na^+, and K^+ transport.

Despite PSS, this method could be introduced to other polymers (i.e., poly sodium allysulfonate (PSAS) and poly 2-acrylamido-2-methylpropane sulfonic acid (PAMPS)) [48–52]. Applying similar protocol, V_{15}/PSAS-Li-1 and V_{15}/PAMPS-Li-1 are obtained proved by SEM, PXRD, FT-IR, Raman and TGA tests (Figs. S54–S55). Remarkably, produced through this powerful PISA method, V_{15}/PSAS-Li-1 and V_{15}/PAMPS-1 display similar 1D nanowire morphology and show excellent ion conductivity performances (e.g., V_{15}/PSAS-Li-1, 3.49 × 10^{-3} S cm^{-1} and V_{15}/PAMPS-Li-1, 3.04 × 10^{-3} S cm^{-1} for Li^+ conductivity at 25 °C) (Fig. S56). Besides, this protocol can be extended to gram-level production. When the reaction conditions are scaled up to ten times, 8.7 g V_{15}/PSS-Li-1 with about 87% yield is obtained (based on Li_7V_{15}, Fig. S57).

4. Conclusions

In summary, we present a series of fast alkali-ion conductor, polymer/polyoxovanadate hybrid nanowires as solid electrolyte by an alternative

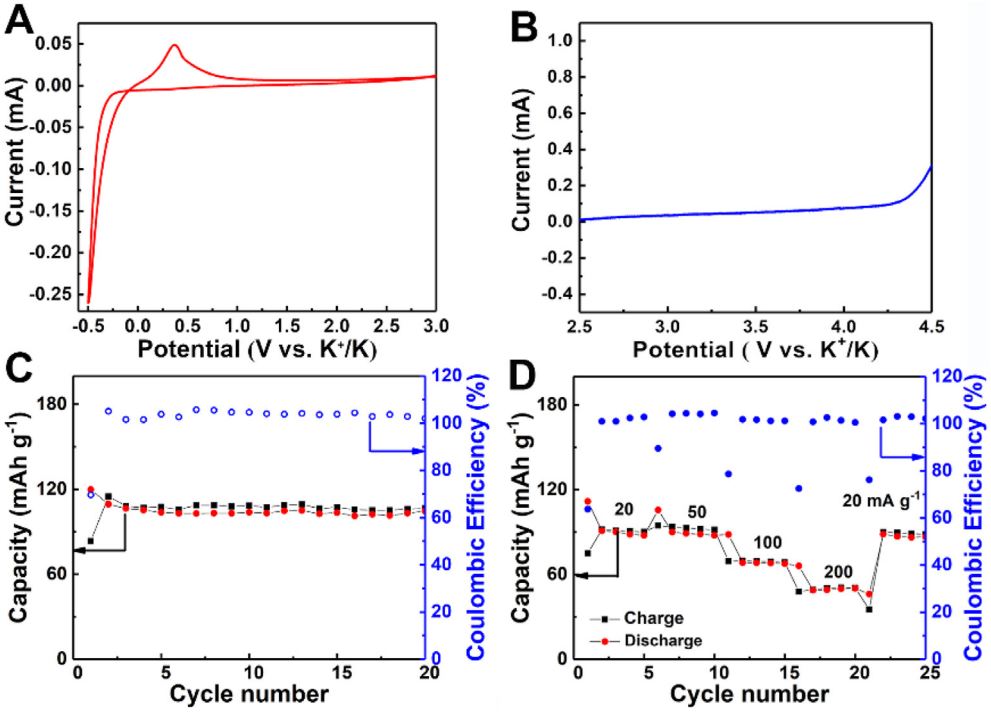

Fig. 5. The CV, LSV plot and solid-state potassium battery tests of V_{34}/PSS-K-1. (A) The plating/striping behavior at scan rate of 1 mV s^{-1}. (B) LSV plot at scan rate of 1 mV s^{-1}. (C) Cycling performance of the solid-state potassium battery at the current density of 20 mA g^{-1}. (D) The rate performances of solid-state potassium at different current densities from 20 to 200 mA g^{-1}.

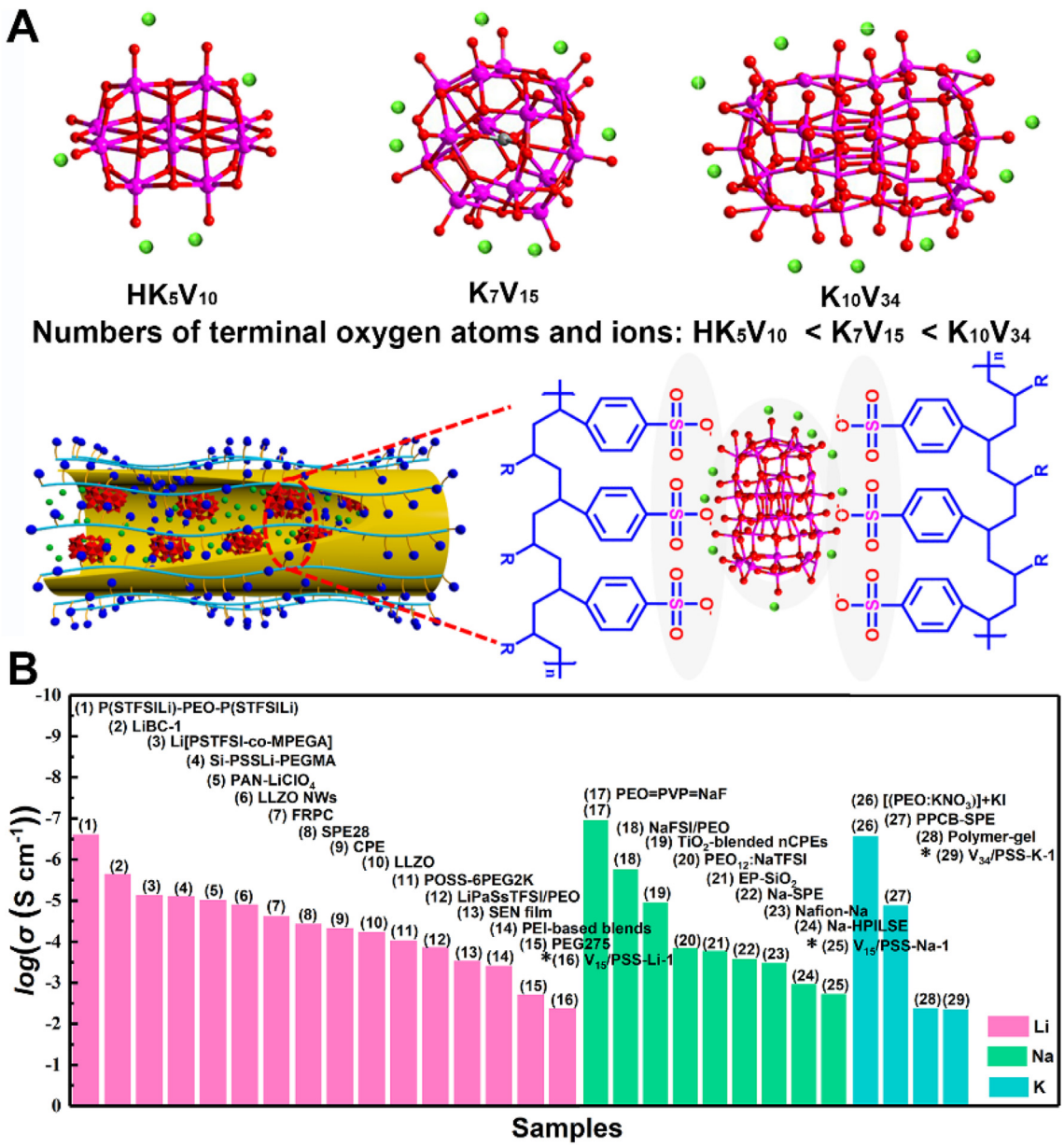

Fig. 6. The mechanism and performances of POVs/PSS. (A) The numbers of terminal oxygen atoms and ions of various POVs and the possible ion transport pathways for POVs/PSS nanowires. (B) Comparison of the ion conductivity among V_{15}/PSS-Li-1, V_{15}/PSS-Na-1, V_{34}/PSS-K-1 and representative polymer based SPE materials (details see Tables S5–S7), asterisk stands for the materials in this work.

facile and scalable polyoxovanadate-induced self-assembly method. POVs/PSS nanowires obtained through this method exhibit excellent uniformity and can provide abundant working ions with high mobility and terminal oxygen atoms (Lewis base sites) to create efficient pathways for ion transport. This method can be extended to various POVs (Li_7V_{15}, HNa_6V_{15}, HK_5V_{10}, K_7V_{15} and $K_{10}V_{34}$) and diverse polymers (e.g., PSS, PSAS and PAMPS) and can be applicable in different ion conductivity (i.e., Li^+, Na^+ and K^+). In addition, a systematically comparative study about the effect of polyoxovanadates indicates that more terminal oxygen atoms and countercations are beneficial for the enhancement of ion conductivity. As result, the POVs/PSS hybrid nanowires with aligned 1D nanowire morphology present ultrahigh Li^+, Na^+ and K^+ conductivity (25 °C, 3.30×10^{-3}, 2.00×10^{-3} and 4.55×10^{-3} S cm^{-1}) with low active energy. Moreover, these POVs/PSS hybrid nanowires exhibit high compatibility with lithium and potassium and high thermal stability can be applied as electrolytes in solid-state batteries with remarkable rate capability and excellent cycling stability ($LiFePO_4$|Li batteries, 148.2 mA h g^{-1} (100 mA g^{-1}), 102.2% retention after 100 cycles; $K_{1.69}Fe[Fe(CN)_6]_{0.90}{\cdot}0.4H_2O$|K batteries, 104.8 mA h g^{-1} (20 mA g^{-1}), 95.6% retention after 20 cycles). This work might open a myriad of opportunities for the development of POMs-based materials in solid electrolytes for the next generation all-solid-state lithium batteries.

Declaration of competing interest

The authors declare that they have no known competing financial interests or personal relationships that could have appeared to influence the work reported in this paper.

CRediT authorship contribution statement

Mi Zhang: Formal analysis, Writing - original draft. **A-Man Zhang:** Writing - original draft, Formal analysis. **Yifa Chen:** Formal analysis. **Jin Xie:** Formal analysis. **Zhi-Feng Xin:** Formal analysis. **Yong-Jun Chen:**

Formal analysis. **Yu-He Kan:** Formal analysis. **Shun-Li Li:** Formal analysis. **Ya-Qian Lan:** Formal analysis. **Qiang Zhang:** Formal analysis.

Acknowledgments

This work was financially supported by NSFC (No. 21871141, 21871142, 21701085, 21825501, U1801257 and 21901122); the NSF of Jiangsu Province of China (No. BK20171032); the Natural Science Research of Jiangsu Higher Education Institutions of China (No. 17KJB150025 and 19KJB150011), National Key Research and Development Program (2016YFA0202500) Project funded by China Postdoctoral Science Foundation (No. 2018M630572 and 2019M651873); Postgraduate Research & Practice Innovation Program of Jiangsu Province (KYCX19_0781). Priority Academic Program Development of Jiangsu Higher Education Institutions and the Foundation of Jiangsu Collaborative Innovation Centre of Biomedical Functional Materials.

Appendix A. Supplementary data

Supplementary data to this article can be found online at https://doi.org/10.1016/j.ensm.2020.04.017.

References

[1] Z. Yang, J. Zhang, M.C. Kintner-Meyer, X. Lu, D. Choi, J.P. Lemmon, J. Liu, Electrochemical energy storage for green grid, Chem. Rev. 111 (2011) 3577–3613.
[2] J.W. Choi, D. Aurbach, Promise and reality of post-lithium-ion batteries with high energy densities, Nat. Rev. Mater. 1 (2016), 16013.
[3] J. Xie, B.-Q. Li, Y.-W. Song, H.-J. Peng, Q. Zhang, A Supramolecular electrolyte for lithium-metal batteries, Batteries & Supercaps 3 (2020) 47–51.
[4] D. Kundu, E. Talaie, V. Duffort, L.F. Nazar, The emerging chemistry of sodium ion batteries for electrochemical energy storage, Angew. Chem. Int. Ed. 54 (2015) 3431–3448.
[5] Y.-H. Zhu, Y.-B. Yin, X. Yang, T. Sun, S. Wang, Y.-S. Jiang, J.-M. Yan, X.-B. Zhang, Transformation of rusty stainless-steel meshes into stable, low-cost, and binder-free cathodes for high-performance potassium-ion batteries, Angew. Chem. Int. Ed. 56 (2017) 7881–7885.
[6] C. Sun, J. Liu, Y. Gong, D.P. Wilkinson, J. Zhang, Recent advances in all-solid-state rechargeable lithium batteries, Nano Energy 33 (2017) 363–386.
[7] A. Manthiram, X. Yu, S. Wang, Lithium battery chemistries enabled by solid-state electrolytes, Nat. Rev. Mater. 2 (2017), 16103.
[8] R. Chen, W. Qu, X. Guo, L. Li, F. Wu, The pursuit of solid-state electrolytes for lithium batteries: from comprehensive insight to emerging horizons, Mater. Horiz. 3 (2016) 487–516.
[9] R. Murugan, V. Thangadurai, W. Weppner, Fast lithium ion conduction in garnet-type $Li_7La_3Zr_2O_{12}$, Angew. Chem. Int. Ed. 46 (2007) 7778–7781.
[10] Y. Shimonishi, T. Zhang, P. Johnson, N. Imanishi, A. Hirano, Y. Takeda, O. Yamamoto, N. Sammes, A study on lithium/air secondary batteries-stability of NASICON-type glass ceramics in acid solutions, J. Power Sources 195 (2010) 6187–6191.
[11] S. Stramare, V. Thangadurai, W. Weppner, Lithium lanthanum titanates: a review, Chem. Mater. 15 (2003) 3974–3990.
[12] P.G. Bruce, S.A. Freunberger, L.J. Hardwick, J.-M. Tarascon, Li-O_2 and Li-S batteries with high energy storage, Nat. Mater. 11 (2011) 19.
[13] C.-Z. Zhao, X.-Q. Zhang, X.-B. Cheng, R. Zhang, R. Xu, P.-Y. Chen, H.-J. Peng, J.-Q. Huang, Q. Zhang, An anion-immobilized composite electrolyte for dendrite-free lithium metal anodes, Proc. Natl. Acad. Sci. U.S.A. 114 (2017), 11069.
[14] E. Quartarone, P. Mustarelli, Electrolytes for solid-state lithium rechargeable batteries: recent advances and perspectives, Chem. Soc. Rev. 40 (2011) 2525–2540.
[15] K.M. Diederichsen, E.J. McShane, B.D. McCloskey, Promising routes to a high Li^+ transference number electrolyte for lithium ion batteries, ACS Energy Lett 2 (2017) 2563–2575.
[16] H. Zhang, C. Li, M. Piszcz, E. Coya, T. Rojo, L.M. Rodriguez-Martinez, M. Armand, Z. Zhou, Single lithium-ion conducting solid polymer electrolytes: advances and perspectives, Chem. Soc. Rev. 46 (2017) 797–815.
[17] Q. Ma, H. Zhang, C. Zhou, L. Zheng, P. Cheng, J. Nie, W. Feng, Y.-S. Hu, H. Li, X. Huang, L. Chen, M. Armand, Z. Zhou, Single lithium-ion conducting polymer electrolytes based on a super-delocalized polyanion, Angew. Chem. Int. Ed. 55 (2016) 2521–2525.
[18] R. Bouchet, S. Maria, R. Meziane, A. Aboulaich, L. Lienafa, J.-P. Bonnet, T.N.T. Phan, D. Bertin, D. Gigmes, D. Devaux, R. Denoyel, M. Armand, Single-ion BAB triblock copolymers as highly efficient electrolytes for lithium-metal batteries, Nat. Mater. 12 (2013) 452.
[19] R. Meziane, J.-P. Bonnet, M. Courty, K. Djellab, M. Armand, Single-ion polymer electrolytes based on a delocalized polyanion for lithium batteries, Electrochim. Acta 57 (2011) 14–19.
[20] W. Liu, S.W. Lee, D. Lin, F. Shi, S. Wang, A.D. Sendek, Y. Cui, Enhancing ionic conductivity in composite polymer electrolytes with well-aligned ceramic nanowires, Nat. Energy 2 (2017) 17035.
[21] S. Chereddy, P.R. Chinnam, V. Chatare, S.P. DiLuzio, M. Gobet, S.G. Greenbaum, S.L. Wunder, An alternative route to single ion conductivity using multi-ionic salts, Mater. Horiz. 5 (2018) 461–473.
[22] S.S. Wang, G.Y. Yang, Recent advances in polyoxometalate-catalyzed reactions, Chem. Rev. 115 (2015) 4893.
[23] X.F. Yuan, C. Sun, J.-N. Duan, J.M. Fan, R.M. Yuan, J.J. Chen, J.-K. Chang, M.S. Zheng, Q.F. Dong, A polyoxometalate-based polymer electrolyte with an improved electrode interface and ion conductivity for high-safety all-solid-state batteries, J. Mater. Chem. 7 (2019) 15924–15932.
[24] X. Meng, H.-N. Wang, S.-Y. Song, H.-J. Zhang, Proton-conducting crystalline porous materials, Chem. Soc. Rev. 46 (2017) 464–480.
[25] T. He, X.B. Xu, B. Ni, H.F. Lin, C.Z. Li, W.P. Hu, X. Wang, Metal-organic framework based microcapsules, Angew. Chem. Int. Ed. 57 (2018) 10148–10152.
[26] J.J. Chen, M.D. Symes, S.C. Fan, M.S. Zheng, H.N. Miras, Q.F. Dong, L. Cronin, High-performance polyoxometalate-based cathode materials for rechargeable lithium-ion batteries, Adv. Mater. 27 (2015) 4649–4654.
[27] A. Müller, R. Rohlfing, J. Döring, M. Penk, Formation of a cluster sheath around a central cluster by a "self-organization process": the mixed valence polyoxovanadate [V34O82]10-, Angew. Chem. Int. Ed. 30 (1991) 588–590.
[28] G. Sheldrick, Crystal structure refinement with SHELXL, Acta Crystallogr. C 71 (2015) 3–8.
[29] G. Sheldrick, Shelxt - integrated space-group and crystal-structure determination, Acta Crystallogr. A 71 (2015) 3–8.
[30] O.V. Dolomanov, L.J. Bourhis, R.J. Gildea, J.A.K. Howard, H. Puschmann, OLEX2: a complete structure solution, refinement and analysis program, J. Appl. Crystallogr. 42 (2009) 339–341.
[31] G. He, L.F. Nazar, Crystallite Size control of prussian white analogues for nonaqueous potassium-ion batteries, ACS Energy Lett 2 (2017) 1122–1127.
[32] Y. Liu, S. Liu, X. Lai, J. Miao, D. He, N. Li, F. Luo, Z. Shi, S. Liu, Polyoxometalate-modified sponge-like graphene oxide monolith with high proton-conducting performance, Adv. Funct. Mater. 25 (2015) 4480–4485.
[33] W. Liu, D. Lin, J. Sun, G. Zhou, Y. Cui, Improved lithium ionic conductivity in composite polymer electrolytes with oxide-ion conducting nanowires, ACS Nano 10 (2016) 11407–11413.
[34] L. Porcarelli, A.S. Shaplov, M. Salsamendi, J.R. Nair, Y.S. Vygodskii, D. Mecerreyes, C. Gerbaldi, Single-ion block copoly (ionic liquid)s as electrolytes for all-solid state lithium batteries, ACS Appl. Mater. Interfaces 8 (2016) 10350–10359.
[35] D. Lin, W. Liu, Y. Liu, H.R. Lee, P.-C. Hsu, K. Liu, Y. Cui, High ionic conductivity of composite solid polymer electrolyte via in situ synthesis of monodispersed SiO_2 nanospheres in poly (ethylene oxide), Nano Lett. 16 (2015) 459–465.
[36] K. Fu, Y. Gong, J. Dai, A. Gong, X. Han, Y. Yao, C. Wang, Y. Wang, Y. Chen, C. Yan, Y. Li, E.D. Wachsman, L. Hu, Flexible, solid-state, ion-conducting membrane with 3D garnet nanofiber networks for lithium batteries, Proc. Natl. Acad. Sci. U.S.A. 113 (2016) 7094–7099.
[37] D. Zhou, R. Liu, J. Zhang, X. Qi, Y.-B. He, B. Li, Q.-H. Yang, Y.-S. Hu, F. Kang, In situ synthesis of hierarchical poly (ionic liquid)-based solid electrolytes for high-safety lithium-ion and sodium-ion batteries, Nano Energy 33 (2017) 45–54.
[38] H. Gao, L. Xue, S. Xin, J.B. Goodenough, A high-energy-density potassium battery with a polymer-gel electrolyte and a polyaniline cathode, Angew. Chem. Int. Ed. 57 (2018) 5449–5453.
[39] K.D. Kreuer, A. Rabenau, W. Weppner, Vehicle mechanism, a new model for the interpretation of the conductivity of fast proton conductors, Angew. Chem. Int. Ed. 21 (1982) 208–209.
[40] L. Shen, H.B. Wu, F. Liu, J.L. Brosmer, G. Shen, X. Wang, J.I. Zink, Q. Xiao, M. Cai, G. Wang, Creating lithium-ion electrolytes with biomimetic ionic channels in metal-organic frameworks, Adv. Mater. 30 (2018), 1707476.
[41] L. Chen, Y. Li, S.-P. Li, L.-Z. Fan, C.-W. Nan, J.B. Goodenough, PEO/garnet composite electrolytes for solid-state lithium batteries: from "ceramic-in-polymer" to "polymer-in-ceramic", Nano Energy 46 (2018) 176–184.
[42] J. Evans, C.A. Vincent, P.G. Bruce, Electrochemical measurement of transference numbers in polymer electrolytes, Polymer 28 (1987) 2324–2328.
[43] Z. Wang, R. Tan, H. Wang, L. Yang, J. Hu, H. Chen, F. Pan, A metal-organic-framework-based electrolyte with nanowetted interfaces for high-energy-density solid-state lithium battery, Adv. Mater. 30 (2018), 1704436.
[44] S.S. Park, Y. Tulchinsky, M. Dinca, Single-ion Li^+, Na^+, and Mg^{2+} solid electrolytes supported by a mesoporous anionic cu-azolate metal-organic framework, J. Am. Chem. Soc. 139 (2017) 13260–13263.
[45] R. Xu, Y. Xiao, R. Zhang, X.-B. Cheng, C.-Z. Zhao, X.-Q. Zhang, C. Yan, Q. Zhang, J.-Q. Huang, Dual-phase single-ion pathway interfaces for robust lithium metal in working batteries, Adv. Mater. 31 (2019), 1808392.
[46] H. Chen, H. Tu, C. Hu, Y. Liu, D. Dong, Y. Sun, Y. Dai, S. Wang, H. Qian, Z. Lin, L. Chen, Cationic covalent organic framework nanosheets for fast li-ion conduction, J. Am. Chem. Soc. 140 (2018) 896–899.
[47] B. Qiao, G.M. Leverick, W. Zhao, A.H. Flood, J.A. Johnson, Y. Shao-Horn, Supramolecular regulation of anions enhances conductivity and transference number of lithium in liquid electrolytes, J. Am. Chem. Soc. 140 (2018) 10932–10936.
[48] N. Byrne, D. MacFarlane, M. Forsyth, Composition effects on ion transport in a polyelectrolyte gel with the addition of ion dissociators, Electrochim. Acta 50 (2005) 3917–3921.
[49] M. Zhu, J. Wu, Y. Wang, M. Song, L. Long, S.H. Siyal, X. Yang, G. Sui, Recent advances in gel polymer electrolyte for high-performance lithium batteries, J. Energy Chem. 37 (2019) 126–142.

[50] B. Yuan, G. Luo, J. Liang, F. Cheng, W. Zhang, J. Chen, Self-assembly synthesis of solid polymer electrolyte with carbonate terminated poly(ethylene glycol) matrix and its application for solid state lithium battery, J. Energy Chem. 38 (2019) 55–59.

[51] X.B. Cheng, C. Zhao, Y. Yao, H. Liu, Q. Zhang, Recent advances in energy chemistry between solid-state electrolyte and safe lithium-metal anodes, Chem. 5 (2019) 74–96.

[52] H. Every, M. Forsyth, D. MacFarlane, Plasticized single conductung polyelectrolytes based on poly (AMPS), Ionics 2 (1996) 53–62.